CLL Resonant Converter With Secondary Side Resonant Inductor and Integrated Magnetics

Yue Liu, Hongfei Wu, *Senior Member, IEEE*, Jun Zou, Yu Tai, and Zixian Ge

***Abstract*—A *CLL* resonant converter with transformer–inductor-integrated magnetics is proposed. The *CLL* resonant converter is derived by placing the resonant inductor of an *LLC* resonant converter on the secondary side of the transformer. In comparison with an *LLC* resonant converter, the circulating current associated with the magnetizing current of the transformer is removed from the resonant inductor. More importantly, the phase difference between the flux in the magnetic cores of the transformer and the resonant inductor becomes larger. Therefore, the flux of the transformer and inductor can be cancelled with each other, resulting in a reduced loss and volume of the magnetic core. A novel structure is proposed to integrate the transformer and inductor with integrated winding structures. Detailed analysis and optimized design of the integrated transformer–inductor are presented. The effectiveness and feasibility of the proposed solutions are verified with simulation and experimental results.**

***Index Terms*—*CLL* resonant converter, magnetic integration, matrix transformer, transformer–inductor integration.**

I. Introduction

THE trend for dc/dc power converters is the pursuing of higher efficiency and higher power density [1], [2]. Among various dc/dc converters, *LLC* resonant converters have been widely concerned by the industry because of their excellent soft-switching performance, low voltage stress of switching devices, and easily achieved magnetic integration [3]–[5]. Despite widely applied in various industry applications, *LLC* resonant converters are still evolving. Many tradeoffs between voltage regulation capability, switching frequency, size/volume of magnetic cores, and efficiency are still necessary to meet the needs of different applications. As a result, new topological variations, modulation strategies, magnetic integration, and implementation methods have been continuously emerging.

Structures of resonant tanks composed of three resonant elements have been studied comprehensively in [6]–[8]. Although similar voltage gain curves can be achieved with some modified resonant tank structures, the *LLC* resonant converter is still the most promising one for industry applications. To push the switching frequency up to several hundreds of kilohertz (kHz) or megahertz (MHz), widebandgap devices, including Silicon carbide (SiC) and gallium nitride (GaN), have been adopted in *LLC* resonant converters [9]–[11]. With the development of widebandgap devices, active power devices are no longer the main factor restricting the power density of *LLC* resonant converters. Compared with active switches, the volume and weight of resonant inductors and transformers have been the major bottlenecks. It has been verified that planar magnetics with printed circuit board (PCB) winding is a high-power density and high-efficiency solution for high-frequency *LLC* converters. However, a high switching frequency of several hundreds of kHz to MHz also brings more challenges to the optimal design of power magnetic components [12]–[14]. The development and challenges of planar magnetics are summarized in [15]. To reduce the huge ac termination loss in high current output applications, the synchronous-rectifiers (SRs) and filter capacitors are integrated with the secondary winding of the transformer [16]. To improve the output current capacity, matrix transformers are adopted by distributing the secondary current to each elemental core [17], [18]. To further reduce the volume and loss, a matrix transformer structure is proposed to integrate four elemental transformers into one magnetic core with a simple four-layer PCB [19]. How to integrate the resonant inductor and the transformer into one magnetic core is another hot topic for high-power density *LLC* resonant converter. A magnetic shunt is used to integrate transformer and inductor in [20]. The magnetic plate is shared by a matrix transformer and a resonant inductor in [21].

Typically, the resonant inductor of an *LLC* resonant converter is placed on the primary side of the converter, as shown in Fig. 1. The circulating current induced by the magnetizing inductance of the transformer will flow through the inductor and lead to

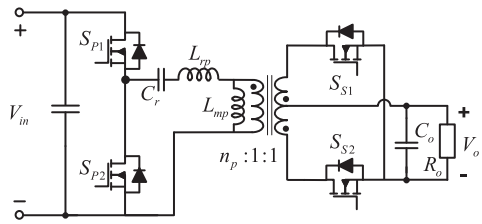

Fig. 1. *LLC* resonant converter.

Manuscript received November 24, 2020; revised January 29, 2021 and April 7, 2021; accepted April 16, 2021. Date of publication April 21, 2021; date of current version June 30, 2021. This work was supported in part by the National Natural Science Foundation of China, under Grant 51977105, in part by the Natural Science Foundation of Jiangsu Province, China, under Grant BK20200017, and in part by the QingLan Project of Jiangsu Province, China. Recommended for publication by Associate Editor H. S. Krishnamoorthy. *(Corresponding author: Hongfei Wu.)*

The authors are with the Center for More-Electric-Aircraft Power System, College of Automation Engineering, Nanjing University of Aeronautics and Astronautics, Nanjing 211106, China (e-mail: liuyue0909@nuaa.edu.cn; wuhongfei@nuaa.edu.cn; zoujun@nuaa.edu.cn; taiyu@nuaa.edu.cn; gzx346002416@nuaa.edu.cn).

Color versions of one or more figures in this article are available at https://doi.org/10.1109/TPEL.2021.3074646.

Digital Object Identifier 10.1109/TPEL.2021.3074646

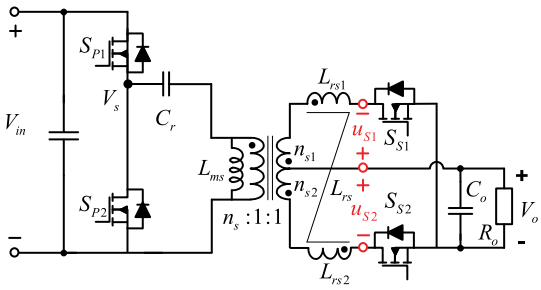

Fig. 2. *CLL* resonant converter.

extra loss. More importantly, the phase difference of the flux generated by the resonant current and magnetizing current is small. Therefore, the benefits from the integration of the resonant inductor and transformer are very limited. In this article, a *CLL* resonant converter with the secondary-side resonant inductor and integrated transformer-inductor is proposed. It is comprehensively evaluated and verified that, in comparison with the *LLC* resonant converter, the *CLL* resonant converter can achieve a better performance.

This article is organized as follows. Section II investigates the gain characteristics of the *CLL* resonant converter and the relationship between it and the *LLC* resonant converter. Section III describes the integration of the core and winding structures based on the *CLL* converter with matrix transformers. Section IV examines the optimization and design of the integrated magnetics. Section V discusses the comparison between the integrated magnetics of the *CLL* and LLC converters. Section VI presents the converter prototype and experimental results. Finally, Section VII concludes this article.

II. *CLL* Resonant Converter

The topology of the *CLL* resonant converter with center-tapped rectifier and resonant inductor on the secondary side is shown in Fig. 2. To ensure that the inductor values in the positive and negative half-cycles are equal, a resonant inductor L_{rs} with two fully coupled windings is employed. As shown in Fig. 2, n_{s1} and n_{s2} are the two secondary windings of the transformer, while L_{rs1} and L_{rs2} are the two windings of the secondary resonant inductor. u_{s1} is the sum of the voltage of n_{s1} and L_{rs1} while u_{s2} is the sum of the voltage of n_{s2} and L_{rs2}. When synchronous rectifier switch S_{S1} is ON, $u_{s1} = V_o$, $u_{s2} = -V_o$, the voltage stress on S_{S2} is twice the output voltage. Similarly, When S_{S2} is ON, $u_{s2} = V_o$, $u_{s1} = -V_o$, the voltage stress on S_{S1} is also twice the output voltage, which is the same as that of an *LLC* resonant converter.

The fundamental harmonic approximation is used for analysis. The primary inverter network of the *CLL* resonant converter can be equivalent to a fundamental sinusoidal voltage source V_s, and the secondary rectifier network is equivalent to a purely resistive load $R_{\rm ac}$, where $R_{\rm ac} = 8{n_s}^2\pi/R_o$. The resonant inductor can be equivalent to the primary side of the transformer. The simplified circuit is shown in Fig. 3.

The main relationships in the *CLL* resonant converter are given in (1)–(6), where f_s is the switching frequency.

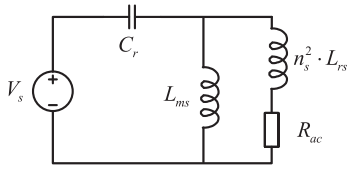

Fig. 3. Equivalent circuit of *CLL* resonant converter.

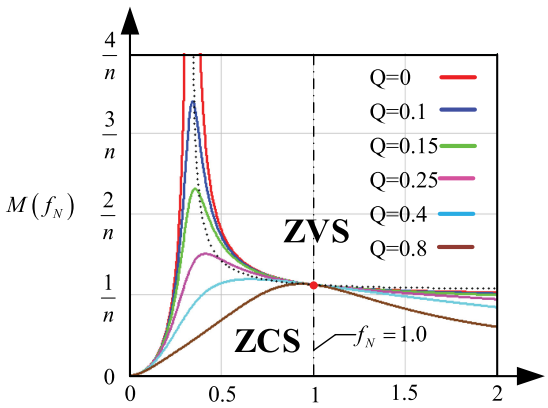

Fig. 4. Voltage gain curves of *CLL* resonant converter.

1) Normalized voltage gain

$$M_{\rm CLL} = 2V_o/V_{\rm in}. \tag{1}$$

2) Resonant frequency

$$f_r = \frac{1}{2\pi\sqrt{L_{\rm ms}//n_s^2 L_{\rm rs}\cdot C_r}}. \tag{2}$$

3) Characteristic impedance

$$Z_0 = \sqrt{\frac{L_{\rm ms}//n_s^2 L_{\rm rs}}{C_r}}. \tag{3}$$

4) Quality factor

$$Q_s = Z_0/R_{\rm ac}. \tag{4}$$

5) The ratio of the magnetizing inductor to the equivalent resonant inductor

$$k_s = \frac{L_{\rm ms}}{n_s^2 L_{\rm rs}}. \tag{5}$$

6) Normalized characteristic frequency

$$f_N = f_s/f_r. \tag{6}$$

Based on the equivalent circuit shown in Fig. 3, the voltage gain expression of the *CLL* converter is deduced as follows:

$$M_{\rm CLL} = \frac{\frac{1}{n_s}\cdot\frac{k_s+1}{k_s}}{\sqrt{\left(\frac{1}{k_s\cdot f_N^2}-\frac{k_s+1}{k_s}\right)^2+\left(Q_s\cdot\frac{(k_s+1)^2}{k_s^2}\right)^2\cdot\left(\frac{1}{f_N}-f_N\right)^2}}. \tag{7}$$

The gain curves of the *CLL* resonant converter are plotted in Fig. 4. The operation regions of *CLL* resonant converters could be divided into two parts. These operation regions are the ZCS region and the ZVS region. As shown in Fig. 4, the characteristics of the *CLL* converter are very similar to that of the *LLC* converter.

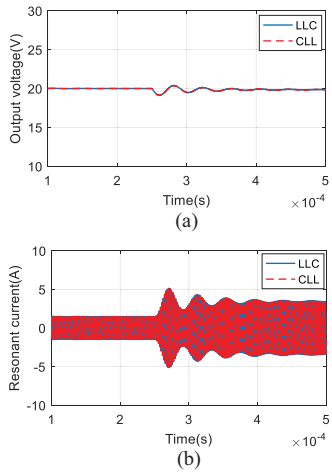

Fig. 5. Simulation waveforms of *CLL* and *LLC* resonant converters with load steps from 20% load to full load. (a) Output voltage. (b) Resonant Current.

The voltage gain expression of the *LLC* resonant converter is deduced as follows:

$$M_{\mathrm{LLC}}=\frac{\frac{1}{n_p}}{\sqrt{\left(\frac{1}{k_p\cdot f_N^2}-\frac{k_p+1}{k_p}\right)^2+Q_p^2\cdot\left(\frac{1}{f_N}-f_N\right)^2}}. \tag{8}$$

where M_{LLC} is the voltage gain, n_p is the transformer ratio of the *LLC* converter, $k_p = L_{mp}/L_{rp}$, and Q_p is the quality factor. According to (7) and (8), if the voltage gain curves of the *CLL* and *LLC* resonant converters are consistent, equivalent conditions are simplified as follows, where $k = k_s = k_p$:

$$\begin{cases} n_s = n_p\cdot\frac{k+1}{k} \\ n_s^2 L_{\mathrm{rs}} = L_{\mathrm{rp}}\cdot\frac{k+1}{k} \\ L_{\mathrm{ms}} = L_{\mathrm{mp}}\cdot\frac{k+1}{k}. \end{cases} \tag{9}$$

If (9) is satisfied, the *CLL* resonant converter and its corresponding *LLC* resonant converter are completely equivalent to each other. Therefore, under the same input and output conditions, the voltage gain characteristics, primary and secondary current of the transformer, resonant capacitor voltage, and other electrical parameters of the two are completely equal.

According to the equivalent condition of *CLL* and *LLC* resonant converters given in (9), once the resonant parameters of the *LLC* converter are determined, the resonant parameters of the corresponding *CLL* converter can be obtained. There has been a lot of research on the optimization of the *LLC* resonant parameters. Optimized parameters of the *CLL* resonant converter can be obtained according to (9) and based on a corresponding *LLC* resonant converter.

To verify the consistency between the *CLL* resonant converter and the *LLC* resonant converter when (9) is satisfied, simulation waveforms of the resonant current and the output voltage under open-loop control when the load steps from 20% load to full load are shown in Fig. 5. It is seen that output voltages and resonant currents of the two resonant converters are completely overlapped with each other, which indicates that the transient response of the *CLL* resonant converter is the same as the *LLC* resonant converter when (9) is satisfied.

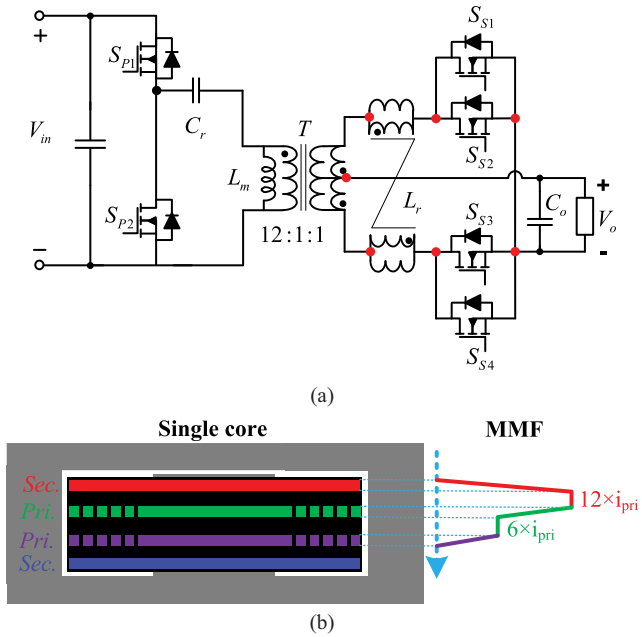

Fig. 6. *CLL* resonant converter with single transformer. (a) Topology. (b) Its MMF with four PCB layers.

Although the external characteristics of the *CLL* and the *LLC* converters are identical when (9) is satisfied, the operations of the transformer and resonant inductor are different. Since the resonant inductor of the *CLL* converter is configured on the secondary side of the transformer, the magnetizing current will not flow through it. Therefore, the core and winding loss of the *CLL* resonant inductor will be reduced.

In terms of the transformer, according to (9), assuming that the number of turns of the secondary winding of the *LLC* transformer is the same as that of the *CLL* transformer, then the number of turns of the primary winding of the *LLC* is $k/k+1$ of the *CLL*. The primary currents of the transformers are the same, so the primary winding loss of the *CLL* transformer will be higher than the transformer in the *LLC* resonant converter. However, the following analysis will indicate that much lower core loss can be achieved with the *CLL* resonant converter and an integrated transformer–inductor structure.

III. Integrated Structure of *CLL* Converter With Matrix Transformers

A resonant converter with high-current output often brings lots of problems. To carry a high current, multiple transformer/inductor windings and SRs with parallel connections are usually used, as shown in Fig. 6(a). The single transformer whose ratio is 12:1 employs a four-layer PCB winding, as shown in Fig. 6(b), where the top and bottom layers are secondary windings and the middle two layers are primary windings. With this structure, high-frequency high *di/dt* ac currents will flow through the secondary common nodes marked by red dots, resulting in large termination loss. Also, the parallel current sharing problem of SRs also needs to be taken seriously enough. Besides, the magnetomotive force (MMF) between primary and

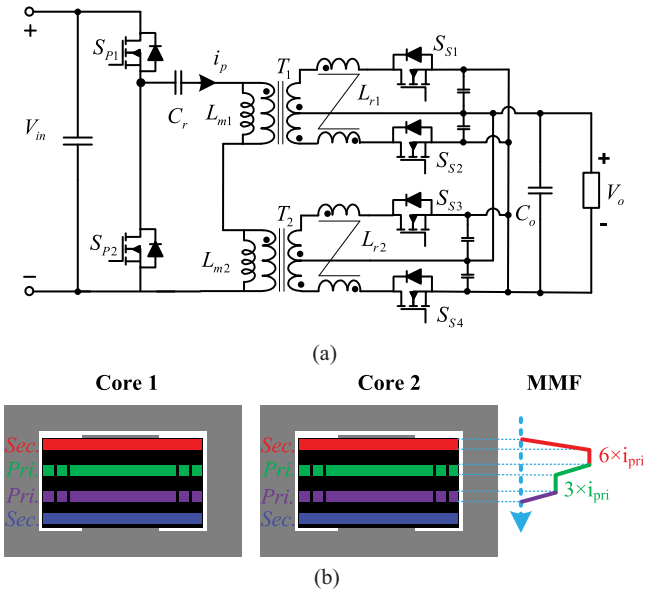

Fig. 7. *CLL* resonant converter with matrix transformers. (a) Topology. (b) Its MMF with four PCB layers.

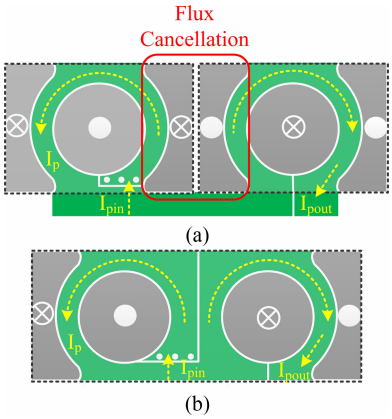

Fig. 8. Primary winding pattern for matrix transformer. (a) Original matrix transformer. (b) Matrix transformer with flux cancellation.

secondary windings is shown in Fig. 6(b). Due to the full-wave structure, when the top layer of secondary windings conducts, the bottom layer does not conduct. Hence, its MMF is 12 times the primary current.

To avoid these problems, the matrix transformer shown in Fig. 7(a) can be employed for the *CLL* resonant converter. By breaking down a single transformer with a ratio of 12:1 into two elemental transformers with a ratio of 6:1, the output power can be evenly distributed. Therefore, as shown in Fig. 7(b), its MMF is only six times of primary current, resulting in low leakage inductor and ac resistance of the winding. Besides, the secondary current of each elemental transformer is balanced due to their primary windings in series connections.

The matrix transformer in Fig. 7(b) can be formed by using two separate ER-cores. The single-turn primary winding winds the middle pillar of each core, as shown in Fig. 8(a) for simplicity. However, this scheme of two ER-cores has an increased volume compared to the single transformer with a single core in Fig. 6(b),

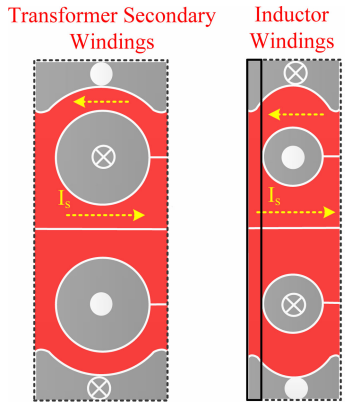

Fig. 9. Separate structure of transformer and resonant inductor.

resulting in extra core loss. To reduce the core size and loss, it can be found that the magnetic flux directions on the adjacent side pillar of the two ER cores are opposite. Therefore, the core structures can be modified, as shown in Fig. 8(b), to achieve flux cancellation and lower termination loss. Compared with the UI core structure presented in [21], the proposed core structure has two side legs, which can significantly reduce the height by 25% while the volume of their magnetic core is almost the same. However, if windings are taken into consideration, the power density of the overall transformer is increased by 17%.

Similarly, the secondary resonant inductor can also adopt this integrated core structure. Originally, a separate structure of the transformer and inductor shown in Fig. 9 would be used. The part of the resonant inductor marked by the solid black box can be removed because its influence on the flux of the transformer is duplicated. Hence, the inductor and transformer can adopt the integrated winding structure instead of the separate structure, as shown in Fig. 10. As shown in Fig. 10(a) and (b), and Fig. 11, regardless of which SR is conducting, there is always one of the secondary windings close to the air gap and another one far from the air gap conducting current. Therefore, the equivalent resonant inductances of the positive half-cycle and negative half-cycle are the same with each other.

In the winding structure of the inductor and transformer, extra leakage flux will be created because the extended secondary windings do not overlap with the primary windings. Fig. 11 shows the cross-sectional view of the integrated winding, which uses a six-layer PCB structure. Among them, the middle two layers are primary windings, and the top and bottom layers are two secondary windings for full-wave rectification. Also, to reduce the influence of the interlayer capacitor between the primary and secondary windings, two shielding layers are used. According to [19], it is suggested that the distance between the winding and the air gap is more than 2.5 times the air gap thickness. In this article, the air gap of the transformer is about 0.1 mm and the air gap of the resonant inductor is about 0.3 mm. To minimize the fringing effect of the air gap, the distance between the top layer winding and the air gap thickness is around 2 mm, which is more than six times the air gap thickness.

Lots of benefits can be achieved through the integrated winding structure in Fig. 10. The footprint of the integrated structure

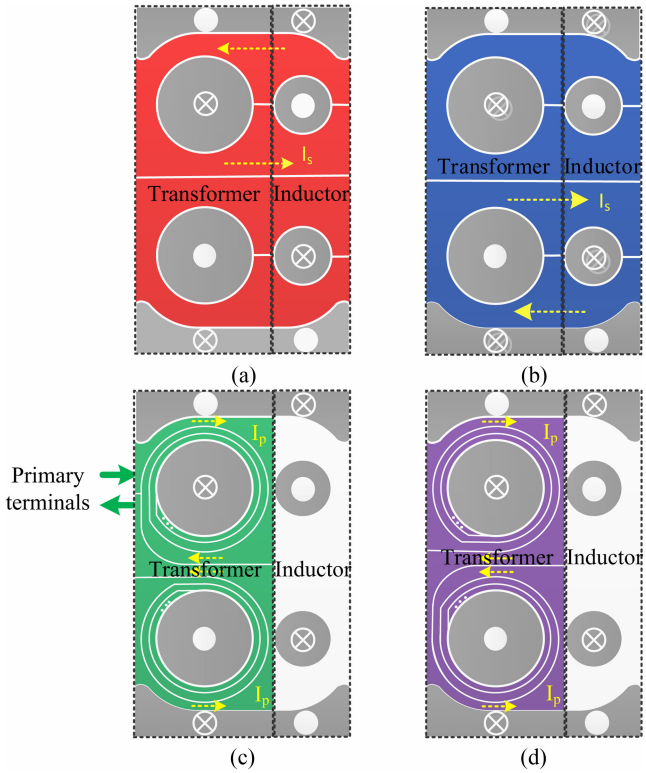

Fig. 10. Integrated transformer and inductor winding structure. (a) Secondary winding for layer 1. (b) Secondary winding for layer 6. (c) Primary winding for layer 3. (d) Primary winding for layer 4.

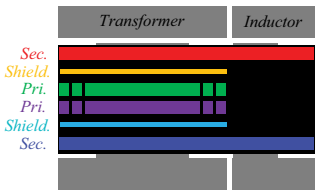

Fig. 11. Cross-sectional view of the PCB winding structure.

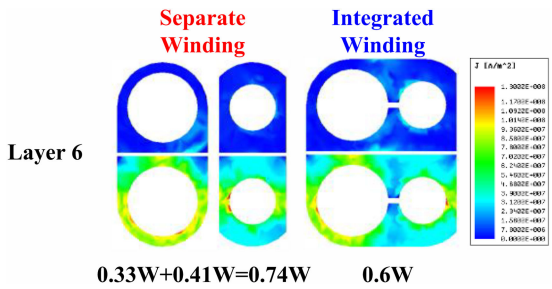

Fig. 12. Comparison of FEA current density simulation results of the separate and integrated winding structures.

is 12% lower than the structure with a separate inductor and transformer. Also, due to the omission of part of the inductor winding, the total winding loss can be greatly reduced. The FEA current density simulation results are shown in Fig. 12. It can be found that the loss of integrated winding is 18.5% lower than the separate winding for secondary portions of layer 6.

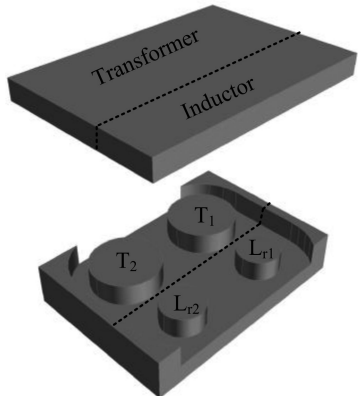

Fig. 13. Integrated core of the transformer and inductor.

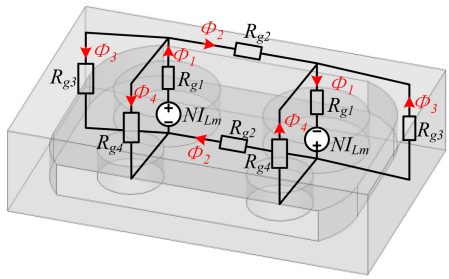

Fig. 14. Simplified reluctance model of the proposed integrated core.

With this exception, the magnetic core of the proposed structure can be integrated into a single core, as shown in Fig. 13. To see the coupling relationship between the transformer and the inductor, the superposition theorem is used for analysis. Fig. 14 shows the reluctance model of the integrated magnetic core only under the excitation of magnetizing current. Among them, R_{g1} and R_{g4} are the air gap reluctance on the transformer and inductor magnetic column, respectively, and R_{g2} and R_{g3} are the magnetic plates and side column reluctance without air gap. After simplification, we can get the following:

$$\begin{cases} \Phi_2 = \dfrac{R_{g3}\cdot R_{g4}}{R_{g2}\cdot R_{g3}+R_{g2}\cdot R_{g4}+R_{g3}\cdot R_{g4}}\cdot\Phi_1 \\ \Phi_3 = \dfrac{R_{g2}\cdot R_{g4}}{R_{g2}\cdot R_{g3}+R_{g2}\cdot R_{g4}+R_{g3}\cdot R_{g4}}\cdot\Phi_1 \\ \Phi_4 = \dfrac{R_{g2}\cdot R_{g3}}{R_{g2}\cdot R_{g3}+R_{g2}\cdot R_{g4}+R_{g3}\cdot R_{g4}}\cdot\Phi_1 \end{cases} \tag{10}$$

where $R_{g2}\approx R_{g3} << R_{g4}$, then $\Phi_4 << \Phi_2 \approx \Phi_3$. Therefore, in the magnetic column, the magnetic flux of the transformer and the inductor are decoupled.

Besides, the transformer and inductor have their own flux component depending on the excitation current of each one of them. By integrating the two magnetic cores into a single core structure, both the inductor and the transformer will share the top and bottom magnetic plates. However, the maximum flux of them occurs at different times, as shown in Fig. 15. The phase difference between the flux can be used. Therefore, the flux density of the integrated magnetic plates is reduced.

As shown in Fig. 15, in the *CLL* resonant converter, the maximum flux of the transformer and the resonant inductor occur at the time t_1 and t_2. The FEA simulation flux distribution results of a separate *CLL* converter and integrated *CLL* converter

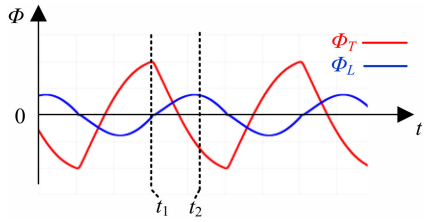

Fig. 15. Flux waveforms of transformer and inductor.

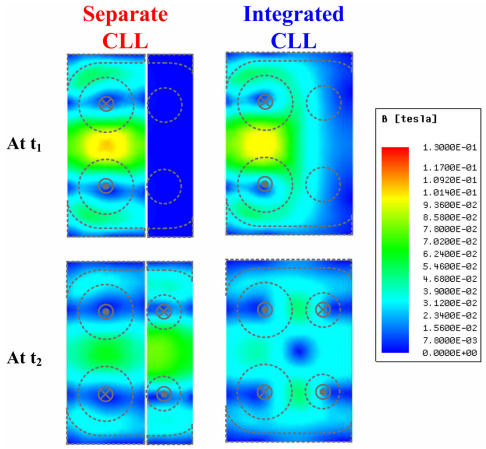

Fig. 16. Comparison of flux density of separate and integrated *CLL* converter.

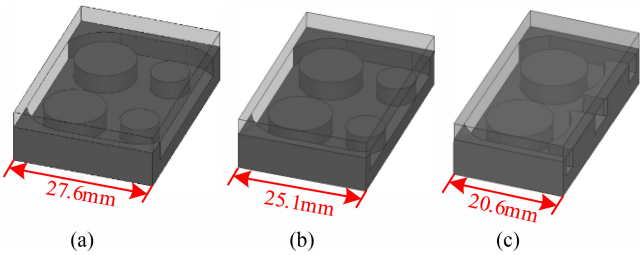

Fig. 17. 3-D views of the integrated cores. (a) Original. (b) After removal. (c) With crescent core.

are compared in Fig. 16. Two structures have the same volume. It is shown that the flux of the integrated structure of the *CLL* converter is more evenly distributed. The core loss is 25% lower compared to the separate structure according to the FEA simulation results.

IV. Optimization and Design for Magnetics

A. Optimization of the Integrated Structure

The top view of the proposed integrated structure in chapter III is shown in Fig. 17(a). Integrating the SRs and output capacitor with the secondary winding reported in [16] can be used to avoid large termination loss. Therefore, the core on the right-hand side of the inductor column, which will affect the heat dissipation of SRs, needs to be removed. The top view of the integrated core after removal is shown in Fig. 17(b). The volume of the core after removal is reduced by around 9%, but its core loss is almost unchanged due to the flux density of the removed portion is very small according to the FEA simulation results.

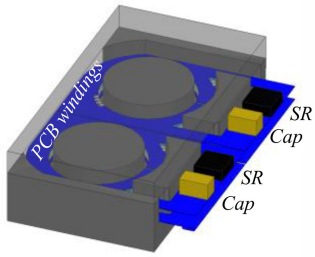

Fig. 18. 3-D view of the integrated magnetics.

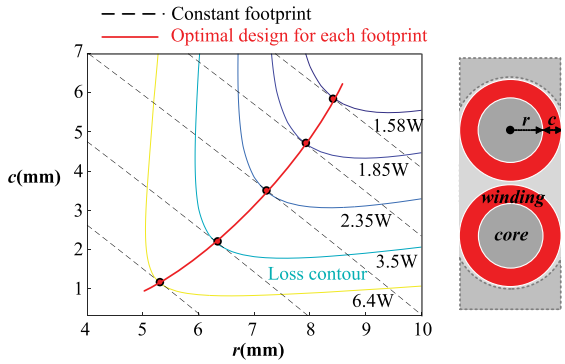

Fig. 19. Loss-footprint curve of the planar integrated transformer.

However, in the structure shown in Fig. 17(b), the difference between the area of the transformer and inductor will cause low utilization of space and winding.

A crescent structure of the resonant inductor is proposed to overcome the abovementioned problem, as shown in Fig. 17(c). The area of the optimized crescent core is the same as before, so its flux density and core loss will not change. After the change, the length of the inductor core is consistent with that of the transformer core while its width is smaller than before. As a result, the volume of the whole integrated magnetics is reduced by around 18% compared to the structure in Fig. 17(b). Besides, to avoid the problem of current accumulation, the four corners of the crescent magnetic are rounded.

According to the FEA simulation results, although the area of the top plate of the crescent structure becomes smaller, the crescent structure has a smaller volume. As a result, compared to the structure before optimization, the core loss of the optimal structure shown in Fig. 17(c) is 6% higher, whereas its volume has a 25% reduction. Therefore, the crescent structure with integrated SRs and filter capacitors shown in Fig. 18 is finally adopted in this article.

B. Design of the Integrated Structure

The design process of the integrated structure is divided into two steps.

1) *Design of the transformer part:* The first step is the design of the transformer part, which is carried out at the target frequency of 500 kHz. The transformer part decided by r and c is designed based on the loss model in [19] and its total loss versus core radius r as the x-axis and secondary winding width c as y-axis can be plotted in Fig. 19. In

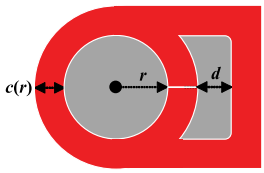

Fig. 20. Different variables in the integrated structure for scanning.

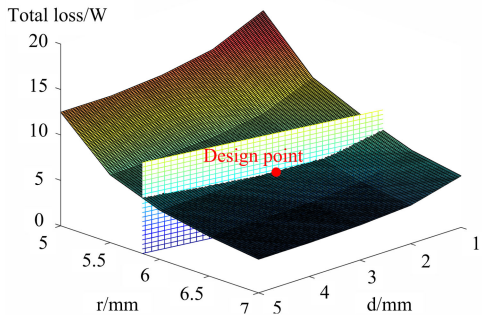

Fig. 21. Integrated magnetics loss with different r and d.

Fig. 19, the constant loss contours are represented by different colored curves and the constant footprint contours are presented by black dot lines. Besides, it should be noted that the red line represents the optimal design under each footprint, and also represents the optimal r–c relationship of the integrated transformer. In this case, winding width c can be expressed as $c(r)$ as following fitting expression:

$$c\,(r) = 0.21 \cdot r^2 - 1.24 \cdot r + 1.8. \tag{11}$$

2) *Design of the integrated structure including the inductor:* Since the inductor loss is affected by many factors and it is not accurate to calculate the inductor loss while still using this loss model, the FEA simulation is used to sweep for the best design of the integrated structure. As shown in Fig. 20, r is the radius of the transformer core, then the width c of the secondary winding is decided by r in (11). Also, the width d of the crescent inductor related to its size and loss is another variable. By sweeping different r and d values, the total losses of the integrated structures are recorded. The final loss surface with core radius r as x-axis and d as y-axis is shown in Fig. 21. The constant volume surface is represented by white with colored lines. On the curve where the volume surface intersects the loss surface, the point marked by red dots with the lowest loss is the optimal design point.

By adopting the above developed design scheme, a good tradeoff between the transformer and the inductor can be achieved.

V. Comparison Between Integrated *CLL* and *LLC* Resonant Converters

Based on the integrated structure and developed design scheme in chapter III and IV, an integrated *LLC* resonant converter is also designed for comparison. The parameters of the *CLL* converter and *LLC* converter are described in Table I,

TABLE I
Specifications of the Proposed *CLL* Converter

	Integrated CLL	Integrated LLC
Resonant frequency	500 kHz	
Transformer turns ratio	12:1	10:1
Primary devices	IGLD60R190D1	
Secondary devices	BSZ037N06LS5	
Primary driver	1EDF5673K	
Secondary driver	FAN3122T	
Resonant capacitor	7 nF	
Resonant inductor	0.12 μH	14.4 μH
Magnetizing inductor	86.4 μH	72 μH

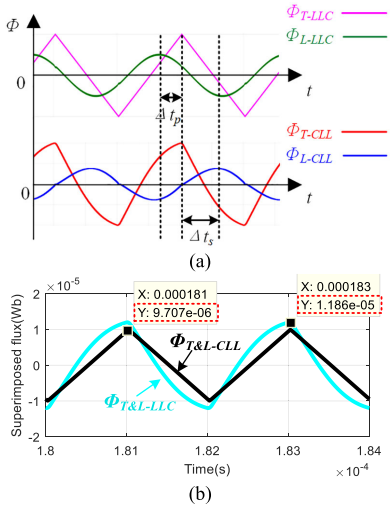

Fig. 22. Flux waveforms of *LLC* and *CLL* resonant converter. (a) Before superimposition. (b) After superimposition.

which satisfy (9). The equivalent resonant inductor of the *CLL* resonant converter is the same as the resonant inductor of the *LLC* resonant converter. It is because of the large turns ratio of the transformer, the inductance of the resonant inductor on the secondary side is much lower than the resonant inductor on the primary side. It has been proved in chapter II that under the equivalent parameter conditions, the electrical characteristics of the *CLL* converter are consistent with those of the *LLC* converter. Therefore, the only difference between the two converters is the magnetic parts. The integrated magnetics of the *LLC* converter share the same volume as the *CLL* converter. However, as shown in Fig. 22(a), it is obvious that the flux phase difference Δt_p between the transformer and the inductor in the *LLC* converter is smaller than 90°. By placing the resonant inductor on the secondary side, the flux phase of the inductor will flip 180°, resulting in a larger phase difference Δt_s. According to (12), the superimposed flux of the transformer and resonant inductor can be calculated. The max superimposed flux of the *CLL* converter is 18% lower than that of the *LLC* converter based on the simulation results, as shown in Fig. 22(b)

$$\phi_{T\&L} = \phi_T + \phi_L = \frac{L_m \cdot I_{Lm}}{N_T} + \frac{L_r \cdot I_p}{N_L}. \tag{12}$$

The flux of the integrated magnetic plate is the result of the superimposition of their flux vectors. Hence, when an integrated

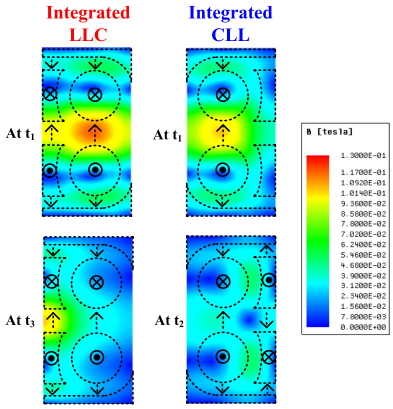

Fig. 23. Comparison of flux density of integrated *CLL* and *LLC* converter.

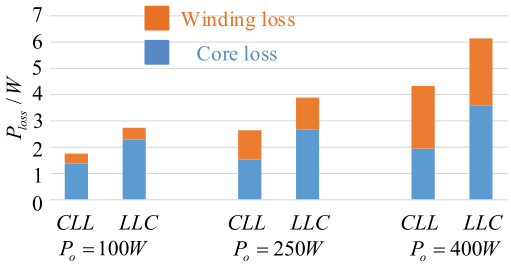

Fig. 24. Loss breakdown comparison of magnetics.

structure is used, better flux cancellation can be achieved by the *CLL* resonant converter resulting in lower core loss. This is beneficial for high-frequency converters due to the core loss accounts for a large proportion.

By importing the simulated current into FEA simulation, the flux distribution results of the integrated *CLL* converter and *LLC* converter are compared in Fig. 23. Two structures have the same volume, but different positions of the resonant inductor. It is shown that the flux of the integrated structure in the *CLL* converter is more evenly distributed. The core loss is 46% lower compared to the integrated structure in the *LLC* converter according to the FEA results. To make a clear comparison between the magnetics parts of the *CLL* converter and *LLC* converter, the loss breakdown of the integrated magnetics under different load conditions is analyzed by FEA simulation, as shown in Fig. 24. Total loss of *CLL* converter is lower than that of *LLC* converter within full load range. However, the loss reduction is mainly achieved by core loss reduction. In terms of winding loss, although the primary winding loss of the transformer is higher for the *CLL* resonant converter, the winding loss of the inductor of *CLL* converter is lower, because the magnetizing current does not flow through it. According to the simulation results shown in Fig. 24, the total winding loss of the *CLL* converter and the *LLC* converter is almost the same.

VI. Experimental Results

Based on the proposed integrated structure and after the optimization, the *CLL* converter is designed and the specifications are described in Table I. To verify the advantage of

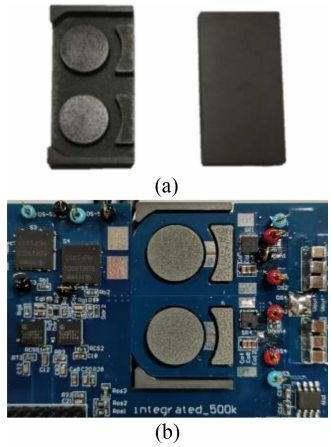

Fig. 25. 500 kHz 400 W 400 V/20 V *CLL* converter prototype. (a) Magnetic components. (b) Prototype without top plate.

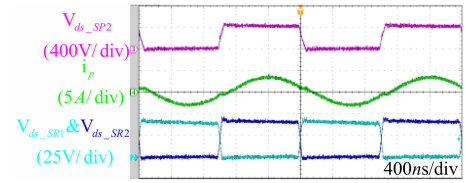

Fig. 26. Experimental waveforms of $V_{\mathrm{ds-SR}}$ for two transformers.

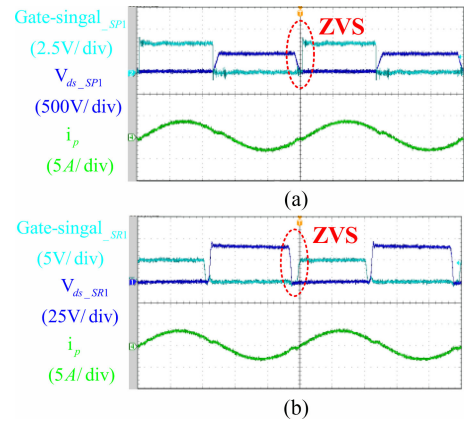

Fig. 27. ZVS waveforms. (a) Primary devices. (b) Secondary devices.

the integrated *CLL* converter, an integrated *LLC* converter with the same volume is tested at the same condition. The resonant parameters of the *LLC* resonant converter are designed first, and then the parameters of the *CLL* resonant converter are obtained according to (9).

The 500 kHz 400 W 400 V/20 V *CLL* converter prototype with the proposed integrated core is shown in Fig. 25. The integrated core has a height of 4 in and a small footprint of 1.24 in^2.

The steady-state operating waveforms under input voltage 400 V and full load are shown in Fig. 26. The waveforms indicate that the voltage stress of SRs is always twice the output voltage. It is also shown that there is no voltage spike on the drain–source voltage of the SRs. Besides, Fig. 27 shows the gate signal and V_{ds} of the devices along with resonant current, which indicates that ZVS can be achieved for both primary and secondary devices.

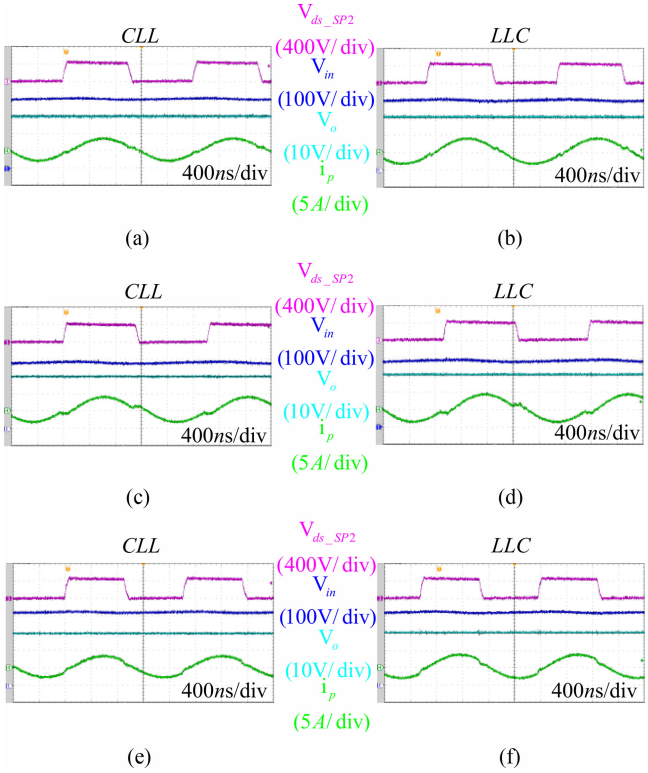

Fig. 28. Resonant converter operating waveforms at full-load conditions with different input voltages. (a) $V_{\rm in} = 400$ V and $f_s = 500$ kHz of *CLL* converter. (b) $V_{\rm in} = 400$ V and $f_s = 500$k Hz of *LLC* converter. (c) $V_{\rm in} = 380$ V and $f_s = 450$ kHz of *CLL* converter. (d) $V_{\rm in} = 380$ V and $f_s = 450$ kHz of *LLC* converter. (e) $V_{\rm in} = 420$ V and $f_s = 550$ kHz of *CLL* converter. (f) $V_{\rm in} = 420$ V and $f_s = 550$ kHz of *LLC* converter.

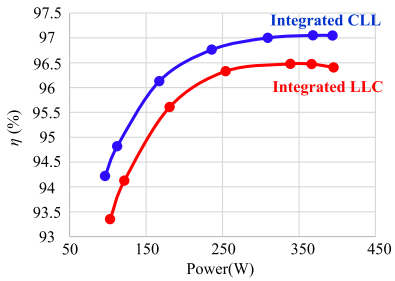

Fig. 29. Measured efficiency.

In this article, the *CLL* resonant converter is used to regulate the bus voltage of front-end PFC whose output voltage is 400 Vdc±20 Vdc. Fig. 28 shows the full-load operating waveforms of the *CLL* converter and the equivalent *LLC* converter. The input voltage $V_{\rm in}$ is from 380 to 420 V, where the frequency is changed from 450 to 580 kHz, respectively, to regulate the output voltage at 20 V. In both cases, ZVS operation is still achieved. Moreover, it is shown that the range of the switching frequency of the *CLL* converter is the same as the *LLC* converter.

The measured efficiency curves of the proposed *CLL* converter and the *LLC* converter are shown in Fig. 29. The proposed *CLL* converter has a peak efficiency of 97.1%, a full-load efficiency of 97.0%, and a light-load (20% load) efficiency of 94.4%. The integrated *CLL* converter helps increase the efficiency by 0.5% at the full-load condition and by 0.9% at light-load. This is because the core loss accounts for the main part during light-load operation. Also, because the magnetizing current does not flow through the secondary-side resonant inductor, the max superimposed flux of the *CLL* resonant converter is always lower than the *LLC* resonant converter within the entire load range. In general, the *CLL* resonant converter with secondary-side resonant inductor is more suitable for high-frequency magnetic integration due to its better flux cancellation.

VII. Conclusion

The *CLL* resonant converter with the secondary-side resonant inductor and integrated magnetics was investigated in this article. By analyzing the voltage gain characteristics of the *CLL* resonant converter, the consistency and difference between the *CLL* resonant converter and the *LLC* converter were analyzed by theories and simulation in detail. The equivalent parameter conditions were also given. To solve the current sharing problem of SRs and reduce the termination loss, a matrix structure was adopted. To reduce the volume and loss of the separate cores, a novel structure with side legs was proposed to integrate the transformer and inductor into a single core. Compared with the *LLC* converter, the larger flux phase difference of the magnetics in the *CLL* resonant converter was utilized to achieve better flux cancellation and lower core loss. Besides, due to the low utilization caused by the difference between the area of the transformer and inductor, a crescent inductor structure was adopted. Without increasing the total loss, the optimized crescent structure had a smaller footprint. Based on the present transformer loss model, a design scheme for the integrated magnetics was developed, which can achieve a good tradeoff between the transformer and inductor. A GaN-based *CLL* converter prototype for 400 V/20 V 400 W was built, which can achieve the efficiency of 97% under full load.

References

[1] J. D. van Wyk and F. C. Lee, "On a future for power electronics," *IEEE J. Emerg. Sel. Topics Power Electron.*, vol. 1, no. 2, pp. 59–72, Jun. 2013.
[2] C. Fei, F. C. Lee, and Q. Li, "A new design paradigm for GaN based LLC converter," in *Proc. IEEE Southern Power Electron. Conf.*, 2017, pp. 1–6.
[3] B. Kim, K. Park, C. Kim, B. Lee, and G. Moon, "LLC resonant converter with adaptive link-voltage variation for a high-power-density adapter," *IEEE Trans. Power Electron.*, vol. 25, no. 9, pp. 2248–2252, Sep. 2010.
[4] B. Yang, F. C. Lee, A. J. Zhang, and G. Huang, "LLC resonant converter for front end DC/DC conversion," in *Proc. IEEE Appl. Power Electron. Conf. Expo.*, Dallas, TX, USA, 2002, pp. 1108–1112.
[5] W. Sun, Y. Xing, H. Wu, and J. Ding, "Modified high-efficiency LLC converters with two split resonant branches for wide input-voltage range applications," *IEEE Trans. Power Electron.*, vol. 33, no. 9, pp. 7867–7879, Sep. 2018.
[6] R. P. Severns, "Topologies for three-element resonant converters," *IEEE Trans. Power Electron.*, vol. 7, no. 1, pp. 89–98, Jan. 1992.
[7] X. Tan and X. Ruan, "Equivalence relations of resonant tanks: A new perspective for selection and design of resonant converters," *IEEE Trans. Ind. Electron*, vol. 63, no. 4, pp. 2111–2123, Apr. 2016.
[8] D. Huang, D. Fu, F. C. Lee, and P. Kong, "High-frequency high-efficiency CLL resonant converters with synchronous rectifiers," *IEEE Trans. Ind. Electron.*, vol. 58, no. 8, pp. 3461–3470, Aug. 2011.
[9] D. Fu, B. Lu, and F. C. Lee, "1 MHz high efficiency LLC resonant converters with synchronous rectifier," in *Proc. IEEE Power Spec. Conf.*, 2007, pp. 2404–2410.
[10] X. Wu, H. Chen, and Z. Qian, "1-MHz LLC resonant DC transformer (DCX) with regulating capability," *IEEE Trans. Ind. Electron.*, vol. 63, no. 5, pp. 2904–2912, May 2016.

[11] B. J. Baliga, "Power semiconductor device figure of merit for high-frequency applications," *IEEE Electron. Device Lett.*, vol. 10, no. 10, pp. 455–457, Oct. 1989.
[12] R. Shafaei, M. C. G. Perez, and M. Ordonez, "Planar transformers in LLC resonant converters: High-frequency fringing losses modeling," *IEEE Trans. Power Electron.*, vol. 35, no. 9, pp. 9632–9649, Sep. 2020.
[13] Z. Ouyang, G. Sen, O. C. Thomsen, and M. A. E. Andersen, "Analysis and design of fully integrated planar magnetics for primary–parallel isolated boost converter," *IEEE Trans. Ind. Electron.*, vol. 60, no. 2, pp. 494–508, Feb. 2013.
[14] Z. Ouyang, O. C. Thomsen, and M. A. E. Andersen, "Optimal design and tradeoff analysis of planar transformer in high-power DC–DC converters," *IEEE Trans. Ind. Electron.*, vol. 59, no. 7, pp. 2800–2810, Jul. 2012.
[15] Z. Ouyang, "Advances in planar and integrated magnetics," Ph.D. dissertation, DTU Elect. Eng. Tech. Univ. Denmark, Denmark, 2011.
[16] D. Huang, S. Ji, and F. C. Lee, "LLC resonant converter with matrix transformer," *IEEE Trans. Power Electron.*, vol. 29, no. 8, pp. 4339–4347, Aug. 2014.
[17] E. Herbert, "Design and application of matrix transformers and symmetrical converters," *presented at High Freq. Power Convers. Conf.*, Santa Clara, CA, USA, May 1990.
[18] K. D. T. Ngo, E. Alpizar, and J. K. Watson, "Modeling of losses in a sandwiched-winding matrix transformer," *IEEE Trans. Power Electron.*, vol. 10, no. 4, pp. 427–434, Jul. 1995.
[19] C. Fei, F. C. Lee, and Q. Li, "High-efficiency high-power-density LLC converter with an integrated planar matrix transformer for high-output current applications," *IEEE Trans. Ind. Electron.*, vol. 64, no. 11, pp. 9072–9082, Nov. 2017.
[20] M. Li, Z. Ouyang, and M. A. E. Andersen, "High-Frequency LLC resonant converter with magnetic shunt integrated planar transformer," *IEEE Trans. Power Electron.*, vol. 34, no. 3, pp. 2405–2415, Mar. 2019.
[21] M. H. Ahmed, A. Nabih, F. C. Lee, and Q. Li, "Low-loss integrated inductor and transformer structure and application in regulated LLC converter for 48-V bus converter," *IEEE J. Emerg. Sel. Topics Power Electron.*, vol. 8, no. 1, pp. 589–600, Mar. 2020.

Yue Liu was born in Jiangsu Province, China, in 1997. He received the B.S. degree in electrical engineering in 2019 from the Nanjing University of Aeronautics and Astronautics (NUAA), Nanjing, China, where he is currently working toward the Ph.D. degree in electrical engineering.

His main research interests include magnetic integration and resonant converters.

Hongfei Wu (Senior Member, IEEE) received the B.S. and Ph.D. degrees in electrical engineering and power electronics and power drives from the Nanjing University of Aeronautics and Astronautics (NUAA), Nanjing, China, in 2008 and 2013, respectively.

Since 2013, he has been with the Faculty of Electrical Engineering, NUAA, where is currently a Professor with the College of Automation Engineering. He has authored and coauthored more than 170 peer-reviewed papers published in journals and conference proceedings. He is the holder of more than 40 Patents. His research interests include high-performance power converters, widebandgap devices applications and magnetic integration.

Dr. Wu was the recipient of the Best Associate Editor of the *Journal of Power Electronics* (2018), the Outstanding Reviewer of the IEEE TRANSACTIONS ON POWER ELECTRONICS (2013), the Changkong Scholar Award and Young Scholar Innovation Award of NUAA (2017). He serves as an Associate Editor of the *Journal of Power Electronics*, *CPSS Transactions on Power Electronics and Applications*, and the *Chinese Journal of Electrical Engineering and Power Electronic Devices and Components*. He is a Guest Associate Editor of the IEEE JOURNAL OF EMERGING AND SELECTED TOPICS IN POWER ELECTRONICS.

Jun Zou was born in Anhui Province, China, in 1996. He received the B.S. degree in electrical engineering from Southeast University (SEU), Nanjing, China, in 2019. He is currently working toward the M.S. degree in electrical engineering with the Nanjing University of Aeronautics and Astronautics (NUAA), Nanjing, China.

His research interests include resonant converters and magnetic integration.

Yu Tai was born in Jiangsu Province, China, in 1998. He received the B.S. degree in electrical engineering in 2019 from the Nanjing University of Aeronautics and Astronautics (NUAA), Nanjing, China, where he is currently working toward the M.S. degree in electrical engineering.

His main research interests include magnetic integration and resonant converters.

Zixian Ge was born in Sichuan Province, China, in 1998. He received the B.S. degree in electrical engineering in 2020 from the Nanjing University of Aeronautics and Astronautics (NUAA), Nanjing, China, where he is currently working toward the M.S. degree in electrical engineering.

His main research interests include magnetic integration and resonant converters.